

Experimental study on bubble dynamics in rod bundle sub-channels using enhanced deep learning*

Heng Zhang,¹ Niujia Sun,¹ Qin Hang,^{1,†} Wencong Wang,² Jiayi Li,¹ and Nuo Xu¹

¹College of Computer Science and Technology, Chongqing University of Posts and Telecommunications, Chongqing 400065, China

²Nuclear Power Institute of China, Chengdu, 610213, China

This study constructed a narrow-spaced rod bundle experimental platform and employed an advanced SF-MR-DST method, which integrates improved Mask R-CNN and DeepSORT algorithms, to systematically investigate the bubble dynamic behavior and void fraction. The experiment focuses on the influence of parameters such as nozzle diameter, flow rate, and shooting height. The results indicate that an increase in flow rate enhances bubble quantity and morphological complexity, with the maximum nozzle diameter being 0.5 mm. The bubble diameter (1.5–4 mm) shows a positive correlation with flow rate, nozzle size, and height, exhibiting a centralized distribution pattern, with approximately 10-20% of the bubbles displaying irregular shapes. Vertical velocity (0.25-0.37 m/s) increases with higher flow rates while exhibiting an initial deceleration followed by acceleration under the influence of nozzle diameters and height, whereas horizontal velocity remains relatively stable at around 0.2 m/s, compared to 0.4 m/s in unconstrained conditions. The void fraction increases nearly linearly with flow rate, with consistent trends across the three methods despite minor discrepancies. This study provides fundamental data and theoretical insights in bubble dynamics for the initialization and operational optimization of experimental reactors, offering significant guidance for enhancing the operational safety and thermal-hydraulic performance of experimental reactor systems.

Keywords: Deep learning, Two-phase flow, Rod bundle channel, Bubble dynamics, Void fraction

I. INTRODUCTION

Rod bundle configurations are widely recognized for their compact design and high thermal conductivity, it has been extensively utilized in various engineering applications, including the reactor cores of pressurized water reactors (PWRs) [1]. Previous studies have shown that reducing the gap-to-diameter ratio (the ratio of gap distance to rod diameter) in rod bundle channels to a critical threshold can significantly alter the void fraction within the channel [2]. Building on this, the present study develops an experimental system to explore the void fraction characteristics in rod bundle channels with a small gap-to-diameter ratio.

In pressurized water reactors (PWRs), to enhance the core outlet temperature and heat transfer efficiency, it is common practice to allow the coolant to undergo subcooled boiling in the hotter regions of the core. However, the bubbles generated during subcooled boiling not only reduce the moderation capability of the core's neutron moderator but also impact the natural circulation capacity of the reactor coolant system, presenting a significant challenge to the stable operation of the reactor [3]. During this process, the generation, migration, and accumulation of bubbles directly affect the flow structure and heat exchange efficiency of the coolant. As such, the study of bubble characteristics and dynamics in air-water two-phase flow is of paramount importance. Among these, the bubble size distribution (BSD) is considered one of the most critical parameters influencing bubble hydrodynamics, and accurate BSD data are essential for precise computational fluid dynamics (CFD) modeling of bubble columns. Additionally, the shape and velocity of the bubbles also influence

the overall fluid dynamics of the system, as they are closely related to drag, lift, bubble wake formation, and path instability [4]. Moreover, by appropriately controlling the void fraction, the reactor's economy, operability, and heat transfer performance can be optimized.

Existing research on bubble dynamics primarily relies on two approaches: invasive and non-invasive methods. Invasive techniques, such as sensors or probes, are limited by their physical interaction with the system, which can disturb the flow and alter bubble behavior, particularly in complex flow conditions [5]. Non-invasive methods, such as imaging and tracking, also face challenges, especially in narrow rod bundle gaps, where optical obstructions and intricate flow patterns hinder accurate observation. Additionally, the presence of spacer grids introduces secondary flows, further complicating bubble tracking. These limitations underscore the need for more advanced techniques to better understand bubble dynamics in such environments.

To address these challenges, this study proposes an innovative approach that integrates deep learning-based image processing algorithms, specifically combining the Mask R-CNN and DeepSORT models, to investigate the dynamic behavior of bubbles in air-water two-phase flow. This method enables precise measurement and statistical analysis of bubble geometric shapes, motion parameters, and void fraction values under various operating conditions. Furthermore, several improvements have been made to the Mask R-CNN model, including optimized anchor box sizes, adjusted loss functions, and reconstructed bubble shapes, to enhance its accuracy in identifying bubbles within the constrained geometry of rod bundle channels.

The structure of this paper is organized as follows. Section II provides a comprehensive overview of the research progress and related work on bubble behavior. Section III details the setup of the experimental apparatus, the configuration of the high-speed camera acquisition system, and the

* Supported by the National Natural Science Foundation of China (No.12005030) and Key Laboratory Fund for Nuclear Reactor System Design Technology (LRSDDT12023108)

† Corresponding author, hangqin@cqupt.edu.cn

experimental conditions. Section IV presents the bubble identification and tracking model, along with the methodologies used to calculate bubble dynamic parameters and void fraction. Section V offers an in-depth theoretical analysis and discussion based on the results obtained in Section IV. Finally, Section VI summarizes the key findings and outlines potential directions for future research.

II. RELATED WORKS

Currently, bubble distribution measurement techniques are primarily categorized into invasive and non-invasive methods [6]. Invasive techniques, such as mesh electrodes [7], offer distinct advantages in obtaining accurate local bubble information and can provide high temporal resolution data. However, these methods require the placement of sensors inside the flow channel, which can disturb the natural motion of the bubbles and affect the measurement results. Additionally, invasive methods are typically limited to local measurements within a two-dimensional plane and lack the capability for multidimensional synchronous detection. In contrast, non-invasive measurement techniques are more flexible and convenient, often utilizing high-speed or infrared cameras to capture images of the bubble flow, which are then analyzed using image processing techniques. These methods avoid disturbing the flow field and can cover a larger measurement area. However, non-invasive methods often encounter issues such as bubble overlap during image processing, which can affect segmentation accuracy and measurement results.

In response to the common issue of bubble overlap encountered during image processing, Zafari [8] proposed a method that utilizes radial symmetry to segment approximately elliptical overlapping objects, making it particularly suitable for silhouette images. On the other hand, Chen [9] introduced a novel technique for processing overlapping bubbles based on fast segmented arc clustering. This method efficiently clusters segmented arcs by detecting major and pair arcs and connecting multi-segment arcs through concave point connection techniques. However, these traditional methods have high demands on image quality and face significant challenges when dealing with complex bubble shapes, bubble clusters, varying lighting conditions, image distortions, and reflections, making them difficult to apply effectively in practical scenarios.

Advances in computer vision and machine learning are addressing the limitations of traditional methods, contributing to reduced analysis time and improved accuracy [10]. In recent years, with the rise of new artificial intelligence techniques, convolutional neural networks (CNNs) have made significant progress and are now widely employed in object detection, semantic segmentation, and instance segmentation. Soibam [11] demonstrated the effectiveness of CNN models in accurately predicting bubble masks and analyzing bubble statistics during mini-channel boiling. Zhou [12] adopted the YOLOv8 model to develop a bubble detection system for supercooled flow boiling, and subsequently integrated various advanced tracking algorithms with the YOLOv8 model to track bubbles. Cui [13] utilized the Mask R-CNN model for bubble

detection and segmentation, enabling pixel-level segmentation masks and accurate descriptions of overlapping bubble shapes. Shi [14] proposed a gas bubble detection and tracking method for gas-driven water microfluidic experiments, based on domain adaptation in deep learning and an enhanced YOLOv8 model.

However, current research on bubble behavior predominantly focuses on individual bubbles under simplified conditions. While valuable, this approach fails to capture the intricate interactions occurring in multi-bubble systems, particularly in confined flow environments such as rod bundle sub-channels. The presence of rods and the interactions among multiple bubbles create highly complex flow patterns, often resulting in irregular, deformable bubble shapes as they ascend through the sub-channels. Existing methods, typically optimized for simpler, individual bubble tracking, are inadequate for addressing the complexities introduced by bubble clustering, rod interference, and flow confinement [15].

In contrast, our proposed approach directly addresses these limitations by providing a more comprehensive framework for studying bubble behavior in rod bundle sub-channels. Unlike conventional methods that struggle with overlapping bubbles, complex shapes, and occlusions, our approach integrates advanced image processing techniques with machine learning models. This combination enables more precise detection, segmentation, and tracking of bubbles in environments with multiple bubbles and rod interference. By focusing on the dynamic interactions among bubbles in a more realistic, grouped configuration, our method offers a deeper and more accurate understanding of bubble dynamics, making it highly suitable for investigating air-water two-phase flow behaviors in complex systems. In the following section, we will detail the construction of an experimental platform specifically designed to explore bubble dynamics in rod bundle sub-channels.

III. EXPERIMENTAL SETUP

A. Hardware

1. Experimental Apparatus

Fig. 1 illustrates the experimental apparatus. It consists of four main components: a rectangular water tank, a rod bundle channel simulator, a bubble generation system, and a computational imaging system. The water tank is made from acrylic glass, with dimensions of 600 mm \times 450 mm for the cross-sectional area and a height of 450 mm. The rod bundle simulation consists of spacer grids, constructed from glass epoxy resin, and the rod bundle, made of aluminum alloy. The spacer grid, sized at 94.7 mm \times 94.7 mm \times 30 mm, provides structural support while ensuring minimal water absorption. The choice of aluminum alloy for the rod bundle is based on its resistance to surface oxidation, which can affect heat transfer properties, as indicated by Wang's research on critical heat flux [16]. The bubble generation system, comprising an adjustable air pump, gas connection tubes, and a

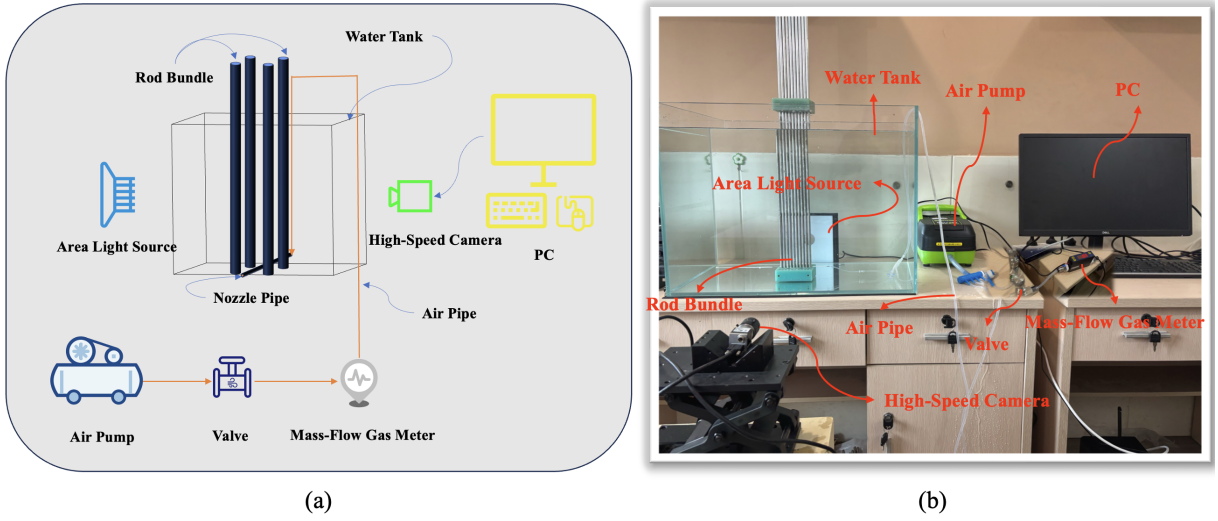


Fig. 1. (a) Schematic diagram and (b) actual picture of the Experimental Facility.

nozzle pipe, introduces air into the coolant to simulate air-water two-phase flow conditions. Finally, the computational imaging system, consisting of a camera, lens, lighting source, and computing unit, captures high-resolution images to analyze bubble dynamics and void fraction distribution within the rod bundle sub-channels, enabling detailed study of air-water two-phase flow behavior.

2. Test Section

The schematic of the narrow-pitch rod-bundle test section is shown in Fig. 2. The rod bundle fuel assembly apparatus is designed based on the actual dimensions and arrangement of real reactor components. To ensure the accuracy of bubble motion detection and computational analysis, only two rows of the rod bundle are used. A 6 mm diameter rod is employed, with a pitch length of 8 mm for the narrow-pitch test sections, enabling the camera to detect gaps as small as 2 mm. The nozzle diameter is adjustable, with available options of 0.3 mm, 0.5 mm, and 0.7 mm. Nozzles are evenly distributed across the gaps between the rods. The air flow rate is adjustable within a range of 0 to 1 L/min. Experiments are conducted at room temperature and atmospheric pressure, with pure water as the liquid phase.

B. Software System

1. High-Speed Image Acquisition System

A typical image acquisition system is composed of camera, lens, light source, and storage software. High-speed cameras enable precise bubble detection through fast frame rates, while the lens ensures optimal focus and clarity. A back illumination technique is employed to enhance bubble outline visibility against the background, improving detection accu-

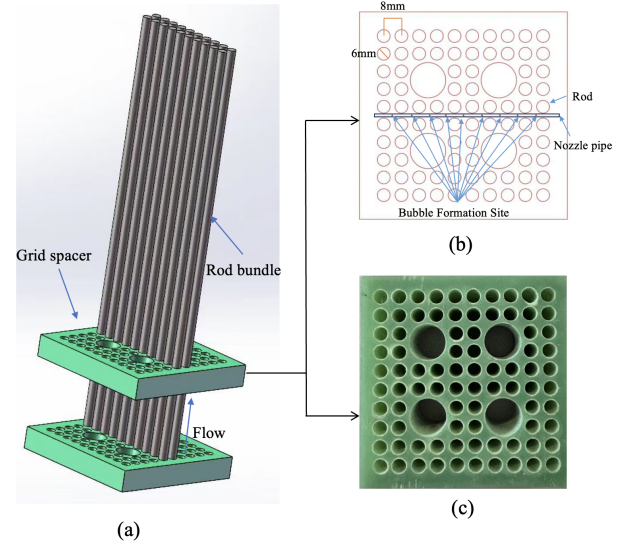


Fig. 2. Experimental test section: (a) 3D model, (b) cross-section and (c) grid spacer.

racy. The light source was selected to ensure consistent and uniform illumination, crucial for capturing clear images of bubbles in dynamic environments. The system utilizes custom storage software built with QT, which interfaces with the camera to acquire images and store them locally for further analysis.

The camera and lens specifications, detailed in Tables 1 and 2, are selected to ensure high-resolution imaging and accurate bubble detection, even in fast-moving flows. Fig. 3 illustrates the acquisition and storage GUI, along with the entire system process, highlighting its functionality for image data capture, management, and high-speed bubble tracking. The system offers an efficient solution for real-time, high-quality imaging under experimental conditions.

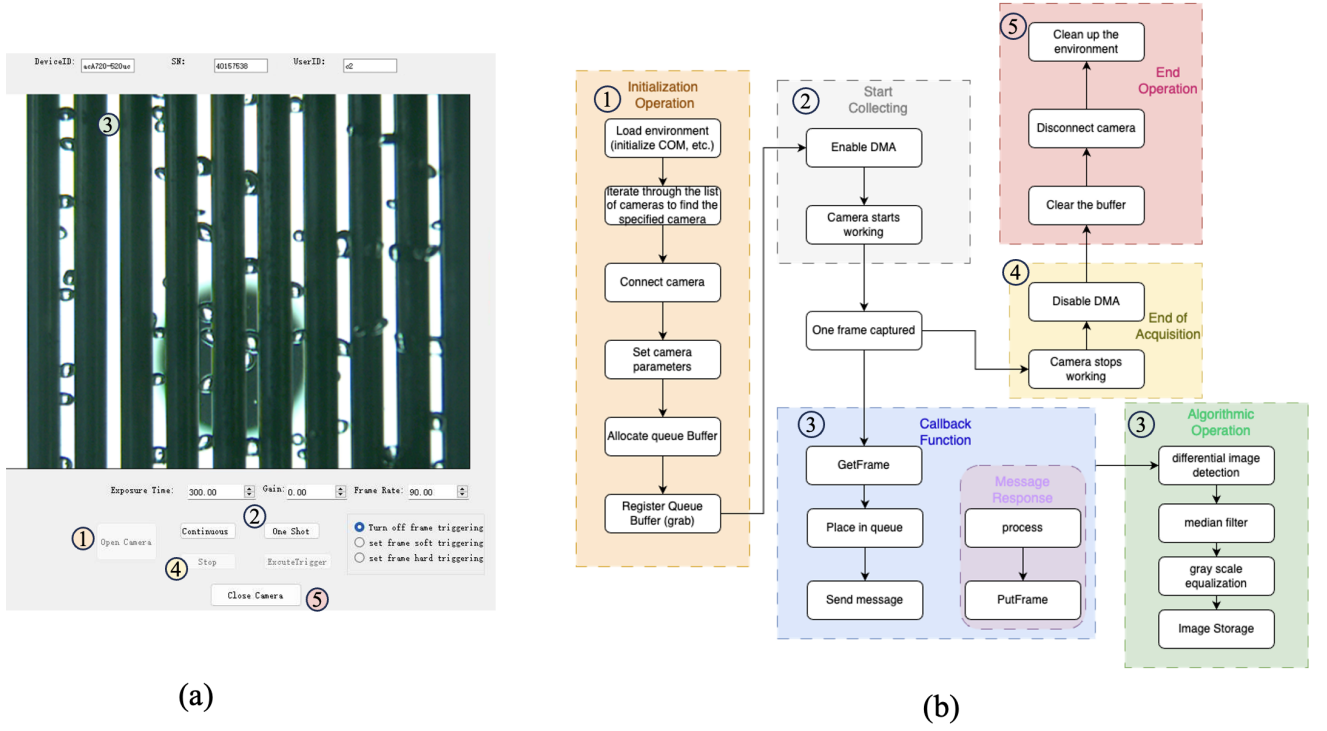


Fig. 3. (a) Interface and (b) Flowchart of the High-Speed Acquisition System.

Table 1. Parameters of camera.

Resolution (H x V)	720 × 540
Sensor Format	1/2.9"
Effective Sensor Diagonal	6.3 mm
Pixel Size (H x V)	6.90 μm × 6.90 μm
Frame Rate	525 fps
Image Data Interface	USB 3.0, 5 Gbit/s
Lens Mount	C-mount

Table 2. Parameters of lens.

Mount	C-mount
Sensor Format	2/3"
Focal Length	16 mm
Working Distance	300 mm
Iris	F1.4 - F16
Iris Type	manual
Pixel Pitch	6.22 μm

Table 3. Combination of nozzle diameter, air flow rate and shooting height.

No.	d_n/mm	$Q_g/(\text{L}/\text{min})$	H	No.	d_n/mm	$Q_g/(\text{L}/\text{min})$	H
1	0.3	0.2	20/100/200	10	0.5	0.5	20/100/200
2	0.3	0.3	20/100/200	11	0.5	0.6	20/100/200
3	0.3	0.4	20/100/200	12	0.5	0.7	20/100/200
4	0.3	0.5	20/100/200	13	0.7	0.2	20/100/200
5	0.3	0.6	20/100/200	14	0.7	0.3	20/100/200
6	0.3	0.7	20/100/200	15	0.7	0.4	20/100/200
7	0.5	0.2	20/100/200	16	0.7	0.5	20/100/200
8	0.5	0.3	20/100/200	17	0.7	0.6	20/100/200
9	0.5	0.4	20/100/200	18	0.7	0.7	20/100/200

220

2. Experimental Parameters Design

221 Bubble images were captured using a Basler high-speed
 222 camera at frame rates of 90 fps with an exposure time of
 223 300 microseconds. The images were taken at three differ-
 224 ent heights: 20mm, 100mm, and 200mm above a fixed base.
 225 A total of 54 experimental conditions were tested, each with
 226 varying nozzle diameters, air flow rates, and shooting heights,
 227 as detailed in Table 3.

228 To ensure the accuracy and reliability of the results, each
 229 experiment included 1000 images per condition, allowing for
 230 statistical validation and comprehensive analysis. Original
 231 bubble images from the experiments, recorded at different air
 232 flow rates, are shown in Fig. 4.

233 With the experimental setup and conditions clearly defined,
 234 we are now ready to apply the SF-MR-DST method to ana-
 235 lyze the collected data and explore the bubble dynamics in the
 236 rod bundle sub-channels.

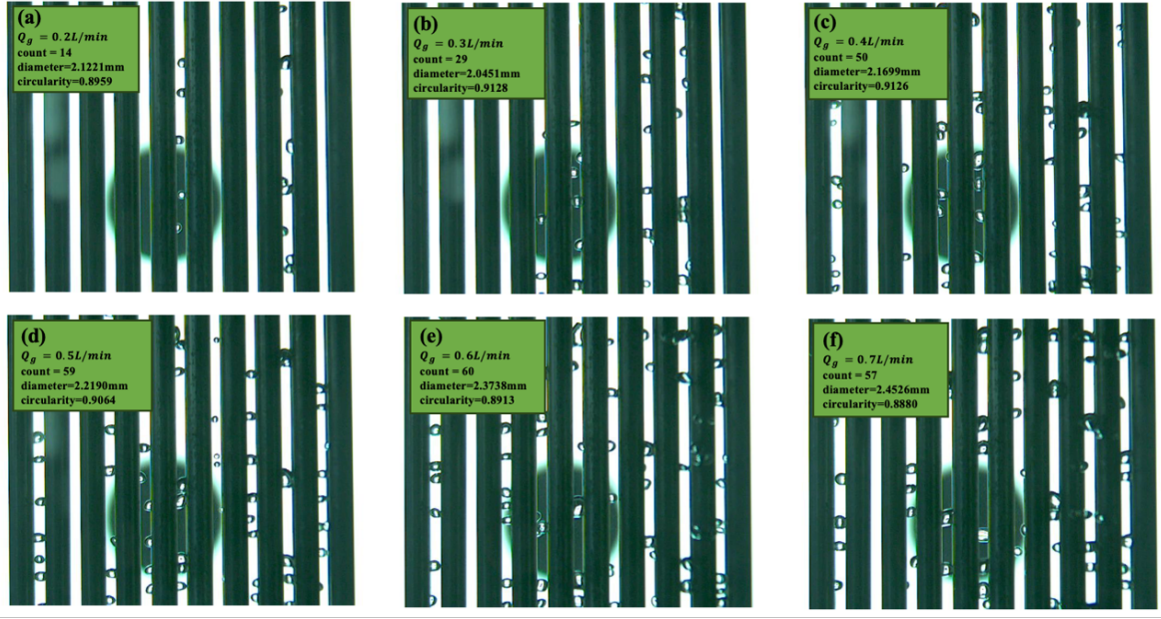


Fig. 4. Original bubble images at different air flow rates with $d_n=0.3\text{mm}$ and $H=20\text{mm}$: (a) $Q_g=0.2\text{L/min}$; (b) $Q_g=0.3\text{L/min}$; (c) $Q_g=0.4\text{L/min}$; (d) $Q_g=0.5\text{L/min}$; (e) $Q_g=0.6\text{L/min}$; (f) $Q_g=0.7\text{L/min}$.

IV. SF-MR-DST METHOD FOR BUBBLE DYNAMICS

The method proposed in this work consists of three main components: detection, tracking, and bubble feature analysis, as illustrated in Fig. 5. The process begins with the raw image data collected by a high-speed camera. Each frame of data is sequentially input into Part I (Improved Mask R-CNN

model) for detection, which outputs the bounding box coordinates for each frame. These coordinates are then fed into Part II (DeepSORT model) for tracking the bubbles. Finally, the detected shapes (reconstructed from the masks output by Part I) and the bubble trajectory data are combined to calculate various dynamic characteristics of the bubbles, such as their quantity, size, shape, and velocity.

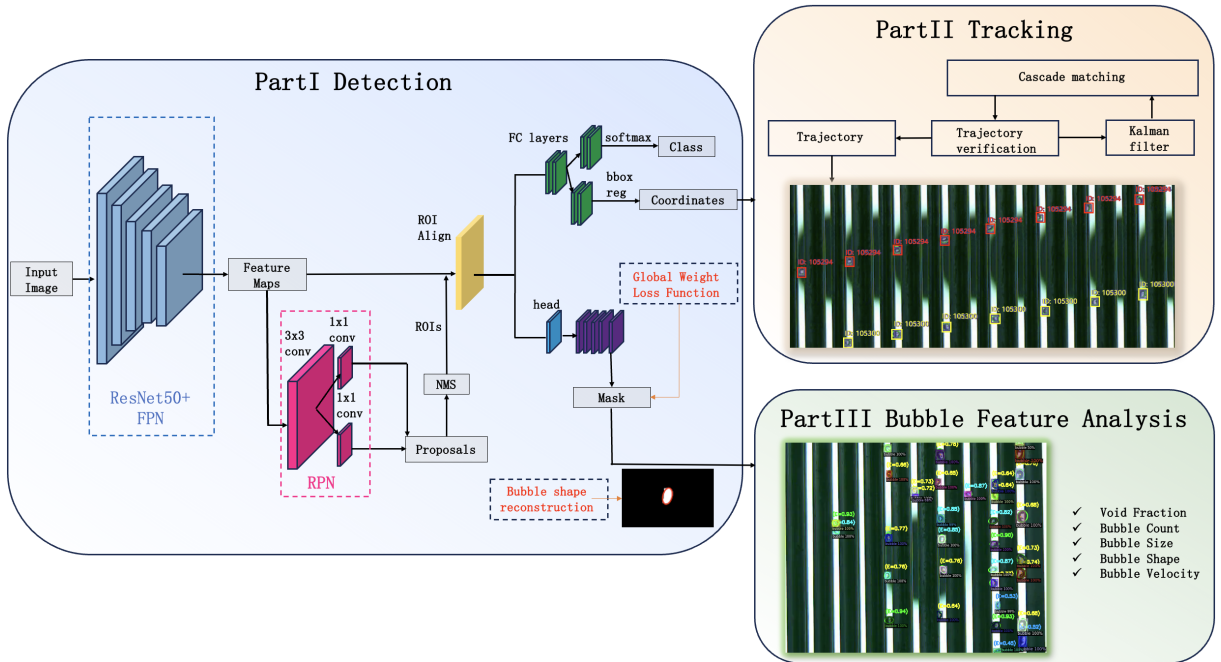


Fig. 5. Schematic diagram of the SF-MR-DST method.

A. Bubble Detection Algorithm

The Mask R-CNN [17] model is employed to extract key feature information from high-speed images. The model adopts ResNet-50 as its backbone network and leverages pre-trained COCO weights for transfer learning. It consists of three main components: feature extraction, region proposal, and detection and segmentation. Firstly, convolutional operations are performed on the input image to extract features, resulting in a series of feature maps at different scales. Next, region proposals are generated based on these feature maps, outputting a set of regions of interest (ROIs) that are likely to contain bubbles. Then, detection and segmentation are performed based on the feature maps and ROIs. This step involves two network heads: one for object classification and bounding box regression, and another for pixel-level mask generation.

To address the challenges posed by the small overall size of bubbles, their susceptibility to occlusion by rod bundles, and the increased recognition time due to the growing number of bubbles with higher air flow rates, we made the following three improvements to the model:

(1) Improvement to the Detection Head

To achieve real-time and efficient bubble detection, we proposed the Fast PConv Head (FPH) method to enhance the detection head of Mask R-CNN. The FPH aims to improve the model's inference speed while maintaining high bubble detection accuracy. The structure of FPH is shown in Fig. 6. It incorporates PConv combined with a 1×1 convolution in the detection head of YOLOv8 [18]. The core principle of PConv is to accelerate convolution operations by computing features only within the local receptive field. Unlike traditional convolutions, PConv focuses only on the pixel features within the local receptive field, rather than considering the entire convolution kernel, thereby effectively reducing computational load and memory usage, and speeding up this stage of computation. The subsequent 1×1 convolution layer integrates and optimizes the features output by PConv without changing the feature map size but adjusting the number of channels, making the feature representation more accurate. This is particularly beneficial for subsequent tasks such as object classification, bounding box regression, and pixel-level mask generation. Especially when dealing with bubble images that are small in size, numerous, and easily occluded, this improved detection head can significantly enhance the model's inference speed while maintaining high detection accuracy, thereby improving the overall performance of Mask R-CNN in handling such bubble images. It enables more efficient bubble detection and segmentation tasks, whether for precise localization and classification of individual bubbles or simultaneous processing of multiple bubbles, all within limited computational resources and with faster, more accurate results.

(2) Improvement to the RPN Network

In this study, since bubbles predominantly exhibit ellipsoidal or spherical shapes, we used three anchor boxes with aspect ratios of 0.5, 1, and 2. In addition to the aspect ratios, the scales of the anchor boxes need to be determined to

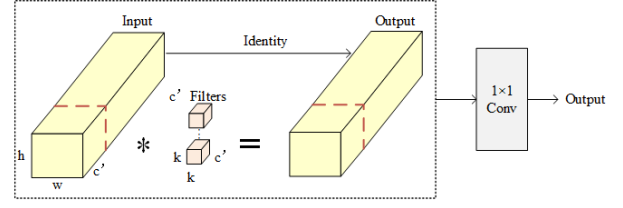


Fig. 6. FPH structure.

match bubbles of different sizes. The bubble sizes in the images range mainly from 6 to 50 pixels. Therefore, we adjusted the anchor box scales to 8, 16, 32, and 64 pixels. This adjustment ensures that the anchor boxes are better suited to capture the varying sizes of bubbles, thereby improving the accuracy of region proposal generation and ultimately enhancing the overall detection performance of the model.

(3) Improvement to the Loss Function

To enhance the model's recognition accuracy for small bubbles to a level comparable with large bubbles, a weight factor was incorporated into the loss function to amplify the contribution of small bubbles to the training loss, as suggested by previous research [19]. The custom weight is defined by Eq. 1, where "size" denotes the equivalent diameter of the bubble, and w is the weight influence factor, which was set to 0.4 in this study. Instead of applying a local weight that impacts each iteration individually, a global weight was implemented using the minimum and maximum bubble sizes from the entire training set. Empirical findings from our experiments indicated that applying weights exclusively to small bubbles yields better results than weighting both small and large bubbles concurrently.

$$\text{Global weight} = \left(\frac{\text{Size}_{\min}^{-1} - \text{Size}_{\max}^{-1}}{\text{Size}_{\min}^{-1} - \text{Size}_{\max}^{-1}} - 0.5 \right) w + 1 \quad (1)$$

B. Bubble Tracking Algorithm

DeepSORT (Deep Simple Online and Realtime Tracking) [20] is a multi-object tracking algorithm based on deep learning, which enhances tracking performance and robustness by integrating Kalman filtering, the Hungarian algorithm, and a cascade matching strategy. In this study, an improved Mask R-CNN algorithm is first employed to identify bubbles in video frames, generating detection bounding boxes. Subsequently, the DeepSORT algorithm is utilized to track multiple bubbles across consecutive frames. DeepSORT not only predicts the position and state of bubbles based on motion features but also addresses occlusion issues to some extent through appearance feature matching, enabling long-term and stable tracking of bubbles. DeepSORT consists of three main modules:

(1) Trajectory Processing and State Estimation

This module employs Kalman filtering to predict and update the motion states of bubbles. Kalman filtering estimates the position, size, and velocity of bubbles, predicting their

Table 4. Performance of the model.

	AP	AP50	AP75	APs	APm	API
before	76.416	98.757	93.128	76.246	89.740	nan
after	82.006	98.760	95.306	81.833	92.546	nan

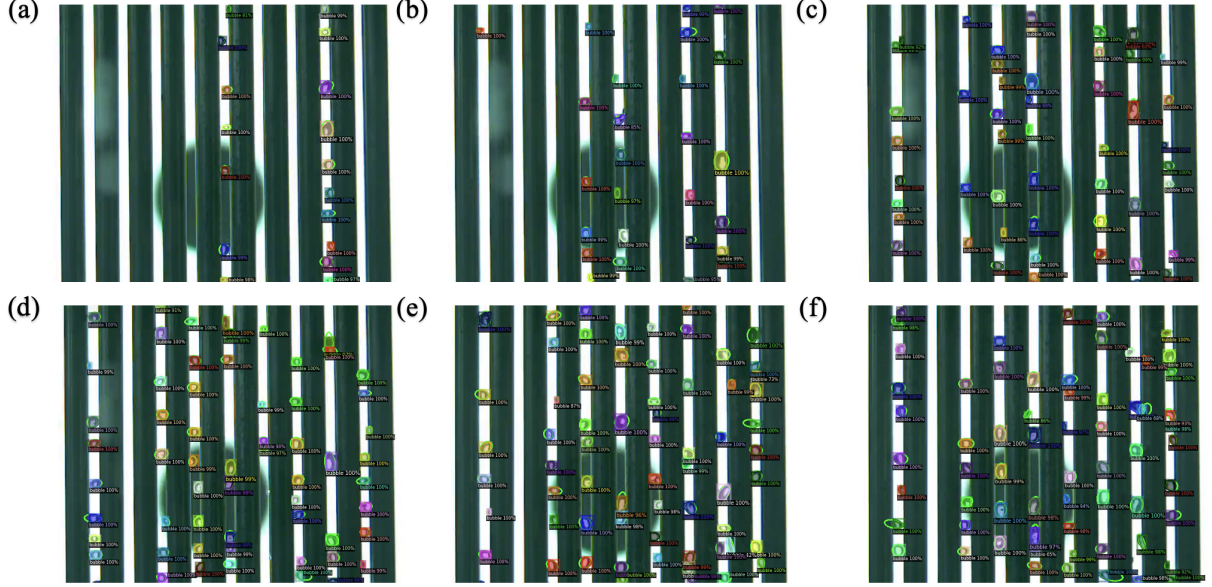


Fig. 7. Detection results at different air flow rates with $d_n=0.3\text{mm}$ and $H=20\text{mm}$: (a) $Q_g=0.2\text{L/min}$; (b) $Q_g=0.3\text{L/min}$; (c) $Q_g=0.4\text{L/min}$; (d) $Q_g=0.5\text{L/min}$; (e) $Q_g=0.6\text{L/min}$; (f) $Q_g=0.7\text{L/min}$.

positions in the next frame and updating these states based on new detection results. This mechanism provides a robust foundation for bubble trajectory prediction, ensuring the continuity and accuracy of tracking.

(2) Assignment Problem Solving

To associate the predicted Kalman states with new detection results, DeepSORT utilizes the Hungarian algorithm to solve the assignment problem. This algorithm constructs a cost matrix by combining motion features (Mahalanobis distance) and appearance features (cosine distance), enabling more precise matching. The Mahalanobis distance measures motion information, while the cosine distance evaluates appearance features. Matching is only performed when both distances meet their respective threshold conditions, effectively preventing erroneous associations caused by occlusion or motion uncertainty.

(3) Cascade Matching

The cascade matching module is designed to address matching issues with different priority levels. This module performs matching according to the priority order of trackers, prioritizing recently matched trajectories and reducing the priority of those that have not been matched for a long time. This mechanism effectively reduces ID switching issues caused by occlusion or targets re-entering the field of view, enhancing the robustness and continuity of tracking. Through the collaborative operation of these three modules, the DeepSORT algorithm not only predicts the position and state of bubbles based on motion features but also resolves occlusion

issues through appearance feature matching, achieving long-term and stable tracking of bubbles. This method demonstrates superior performance in bubble detection and tracking tasks within high-speed images, providing strong support for bubble behavior analysis.

C. Bubble Feature Analysis

1. Bubble Shape Classification

Based on the mask outputs from the model described in Section IV A, we can perform bubble feature analysis and extraction. According to the relationship between bubble shape and aspect ratio, bubbles can be roughly classified into the following categories: spherical bubble ($0.9 < E \leq 1$), ellipsoid bubble ($0.8 < E \leq 0.9$), oblate bubble ($0.6 < E \leq 0.8$), skirt bubble ($0.3 < E \leq 0.6$), and strongly deformed bubble ($E \leq 0.3$). The aspect ratio, denoted by E , is defined and calculated by Eq. 2, where w and h represent the lengths of the major and minor axes of the ellipse, respectively, that has the same normalized second central moments as the region.

$$E = \frac{h}{w} \quad (2)$$

2. Bubble Fitting and Size Calculation

After analyzing the shape feature distribution of the bubbles, further processing is required to calculate the corresponding diameter of each bubble. Based on observations of the bubble shape distribution from a large amount of experimental data, approximately 70% of the bubbles follow the assumption of an ellipsoidal shape. Therefore, we performed both elliptical fitting based on region extraction and elliptical fitting based on contour points for the masks output by the model described in Section IV A. It was found that the elliptical fitting based on contour points more closely matches the actual bubble shape, to some extent, helps eliminate bubble information loss caused by rod bundle occlusions. This improves the accuracy of subsequent void fraction calculations. To better compare the size calculation results after fitting, we calculated the equivalent bubble diameters under the assumptions of a sphere (d , Eq. 3) and an ellipsoid (d_e , Eq. 4), as well as the sauter mean bubble diameter (d_s , Eq. 5) based on the experimental data. Here, S represents the area of the region (i.e., the number of pixels of the region scaled by pixel area), L_t is the height of the imaging segment measured using a scale, and L_p is the camera's vertical resolution, w' and h' represent the lengths of the major and minor axes of the ellipse from the contour-point-based elliptical fitting.

$$d = \sqrt{S \cdot \left(\frac{L_t}{L_p}\right) \cdot \left(\frac{L_t}{L_p}\right) / \pi} \quad (3)$$

$$d_e = \sqrt[3]{\left(w' \cdot \left(\frac{L_t}{L_p}\right)\right)^2 \cdot \left(h' \cdot \left(\frac{L_t}{L_p}\right)\right)} \quad (4)$$

$$d_s = \frac{\sum_{i=1}^N n_i d_{e,i}^3}{\sum_{i=1}^N n_i d_{e,i}^2} \quad (5)$$

3. Bubble Velocity Calculation

Based on the bubble tracking outlined in Section IV B, we obtain a series of trajectories corresponding to various bubble IDs. Due to the indistinct characteristics of the bubbles and the high degree of overlap under certain experimental conditions, misidentifications of bubbles can occur. To ensure more accurate bubble velocity data, we performed a cleaning process on the identified bubble trajectories. This process retained only those bubble IDs that had more than three data points and continuous frame sequences, and where the y-axis velocity was non-zero. After cleaning the data, we can then calculate the true velocity of each remaining bubble ID.

The true velocity can be computed based on the scale of the real-world field of view. The velocity is decomposed into two components: the lateral velocity (horizontal velocity in the left-right direction) and the vertical velocity (rise velocity along the upward direction). By utilizing these components,

we can derive the precise bubble velocity, which reflects both the movement in the horizontal plane and the vertical direction.

4. Void Fraction Calculation

The void fraction (α), as a critical parameter, is typically calculated using image processing methods, with two common approaches: the area method [21] and the volume method [22]. The area method calculates the void fraction by counting the number of bubbles and their areas. It can be computed as defined in Eq. 6, where: α_n is the pixel area of the n-th bubble after image segmentation and shape fitting; A is the total real cross-sectional area of the flow channel. The volume method, on the other hand, calculates the void fraction by considering the number of bubbles and their volumes. It can be computed as defined in Eq. 7, where: v_i is the pixel volume of the i-th bubble after image segmentation and shape fitting; V is the total real volume of the flow channel.

$$\alpha = \frac{\sum \left(a_n \cdot \left(\frac{L_t}{L_p}\right) \cdot \left(\frac{L_t}{L_p}\right) \right)}{A} \quad (6)$$

$$\alpha = \frac{\sum \left(v_i \cdot \left(\frac{L_t}{L_p}\right) \cdot \left(\frac{L_t}{L_p}\right) \cdot \left(\frac{L_t}{L_p}\right) \right)}{V} \quad (7)$$

To validate the feasibility of the above calculation methods, we also calculated the void fraction based on the actual air intake volume [23]. This is defined by Eq. 8 below, where t represents the bubble rise time, which is obtained from the true velocity in the y-axis direction as calculated in Section IV C 3, as well as the height of the imaging segment measured using a scale. Q_g denotes the air flow rate indicated by the air flow meter, and V is the total real volume of the flow channel.

$$\alpha = \frac{Q_g \cdot t}{V} \quad (8)$$

Fig. 8 shows the selected target width and target bottom area used in calculating the actual area and volume of the flow path. The height of both is the camera's field of view height.

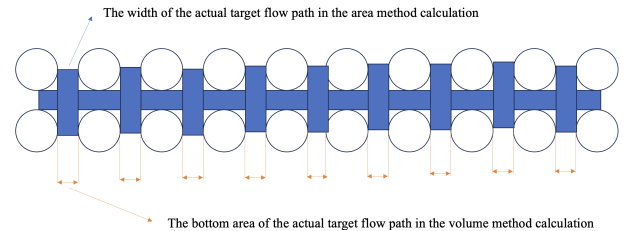


Fig. 8. Target Width and Target Bottom Area for Flow Path.

V. RESULTS AND DISCUSSION

A. Bubble Dynamics

1. Shape and Size Distribution

Fig. 9 illustrates the proportion of bubbles of different shapes in the total bubble distribution, calculated using the aspect ratio formula (Eq. 2 in Section IV C 1), under various operating conditions. The y-axis also displays the number of

bubbles of different shapes. By comparing groups (a, b, c), (d, e, f), and (g, h, i), it is evident that nozzle diameter significantly influences bubble formation. The smallest proportion of irregular bubbles occurs at a 0.3 mm nozzle diameter, while the largest proportion is observed at 0.5 mm, with intermediate values at 0.7 mm. Comparing groups (a, d, g), (b, e, h), and (c, f, i), it can be seen that as bubble rise height increases, both the number of bubbles and the proportion of irregular bubbles decrease. Additionally, higher flow rate leads to more bubbles and a greater proportion of irregular bubbles.

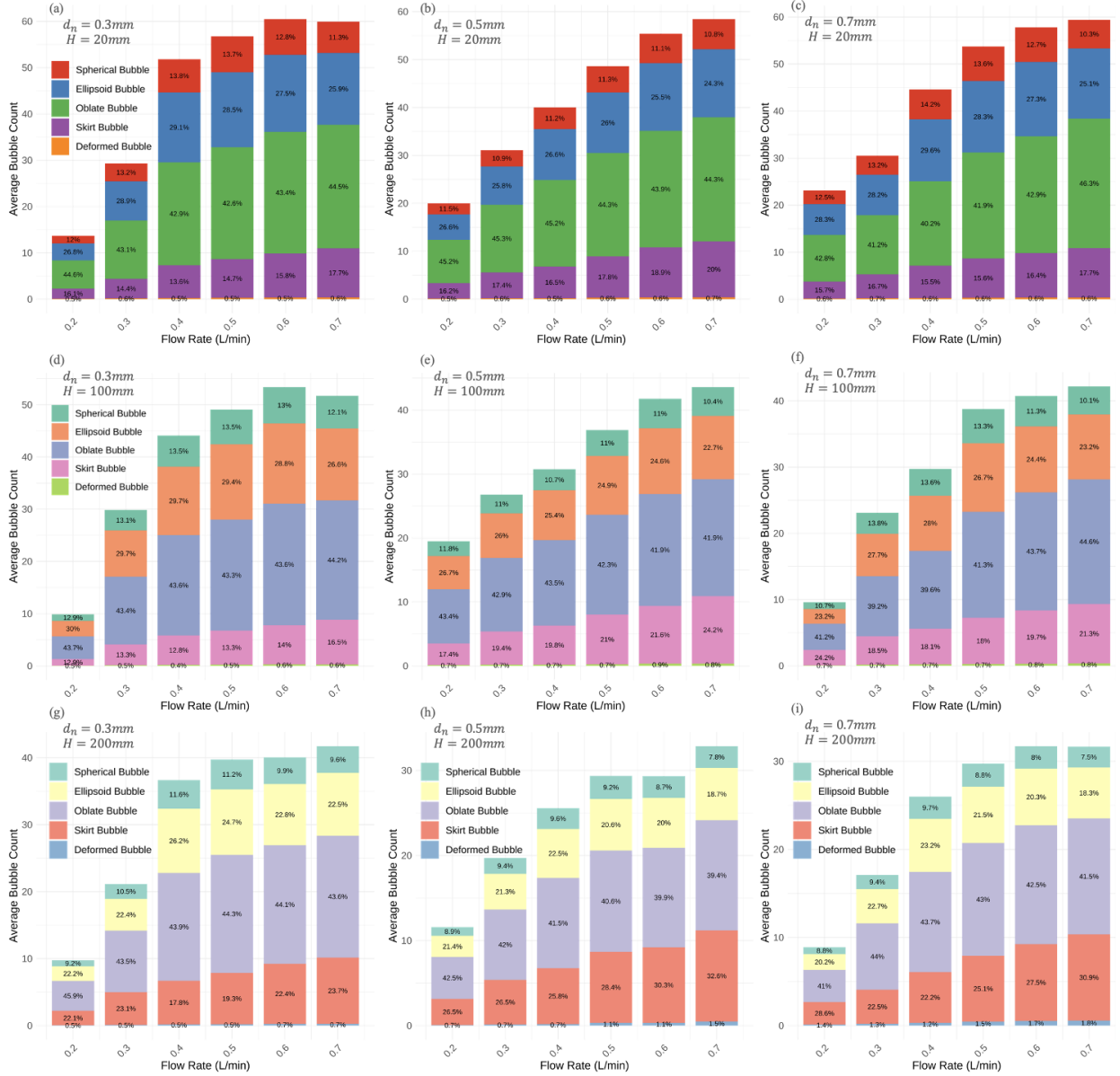


Fig. 9. Histogram of Bubble Counts Classified by Aspect Ratio.

Fig. 10 shows the distribution of average equivalent bubble diameters, calculated using spherical and ellipsoidal assumptions (Eq. 3.4.5 in Section IV C 2), and Sauter mean diameters under different operating conditions. Comparing groups (a, b, c), (d, e, f), and (g, h, i), bubble diameter generally increases with nozzle diameter. Comparing groups (a, d, g), (b, e, h), and (c, f, i), bubble diameter tends to increase with rise height. It also shows an overall increasing trend with flow rate.

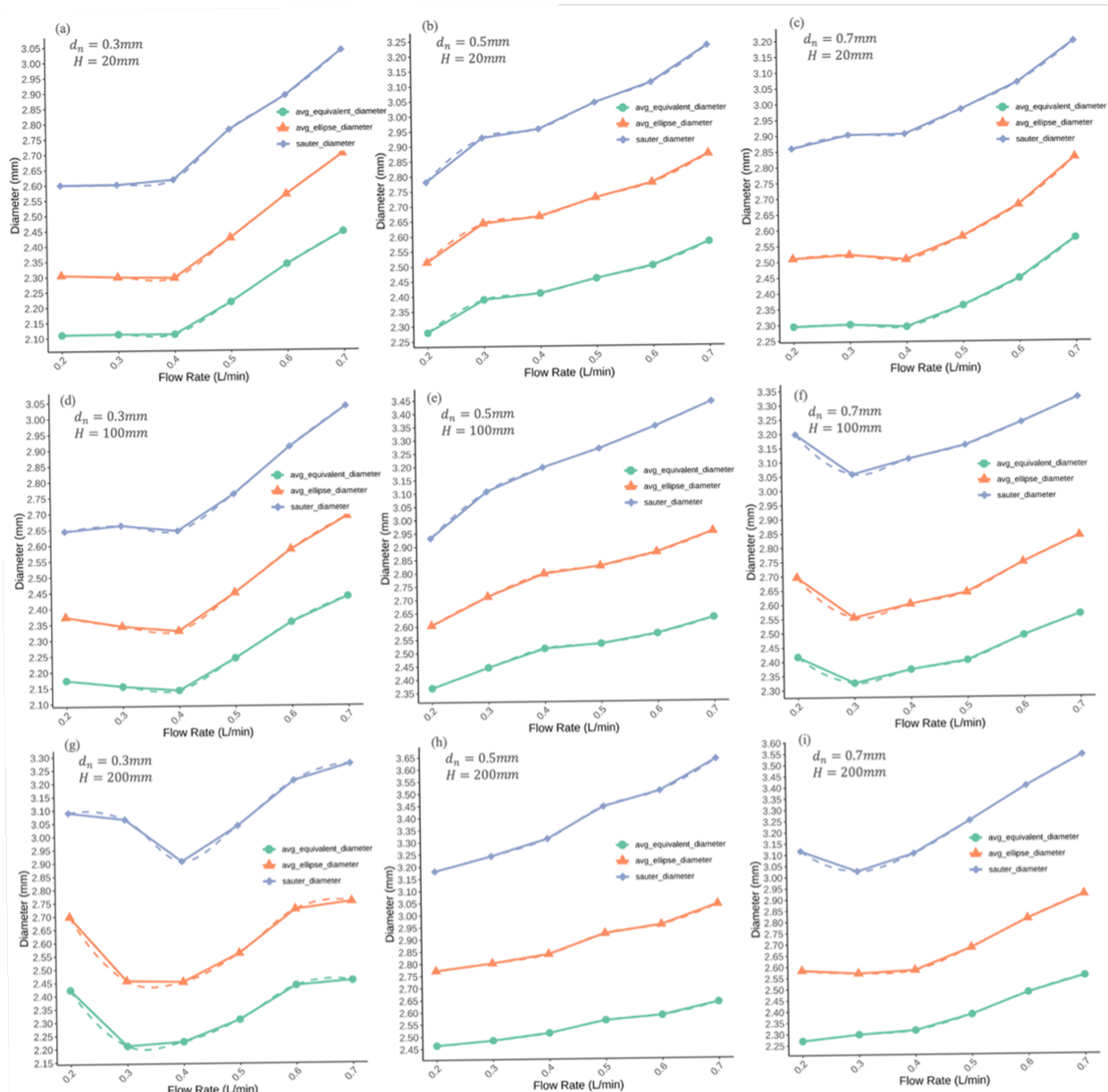


Fig. 10. Average Equivalent Bubble Diameters and Sauter Mean Diameters.

Fig. 11 displays the probability density distribution of bubble diameters, calculated using the ellipsoidal assumption (Eq. 5 in Section IVC 2). The distribution reveals a bell-shaped curve, indicating that most bubbles tend to cluster around a central diameter value.

When comparing groups (a, b, c), (d, e, f), and (g, h, i), it is evident that the peak of the distribution, which represents the most probable bubble diameter, decreases as the nozzle diameter increases. This implies that larger nozzle diameters (0.5mm, 0.7mm) promote a broader range of bubble sizes, reducing the dominance of any single diameter. Similarly, when examining groups (a, d, g), (b, e, h), and (c, f, i), the peak of the distribution also diminishes with increas-

ing rise height. This trend suggests that as bubbles travel higher through the medium, their sizes become more dispersed. Moreover, as the flow rate increases, the peak of the distribution becomes more pronounced, and the range of bubble diameters narrows. This indicates that higher flow rates tend to produce more uniform bubble sizes.

Additionally, by examining the maximum and minimum bubble diameter ranges for each operating condition, it is evident that as flow rate, nozzle diameter, and bubble rise height increase, the bubble diameter tends to increase. This observation reinforces the results shown in Fig. 10. These trends offer valuable insights into the complex relationship between operating conditions and bubble size distribution.

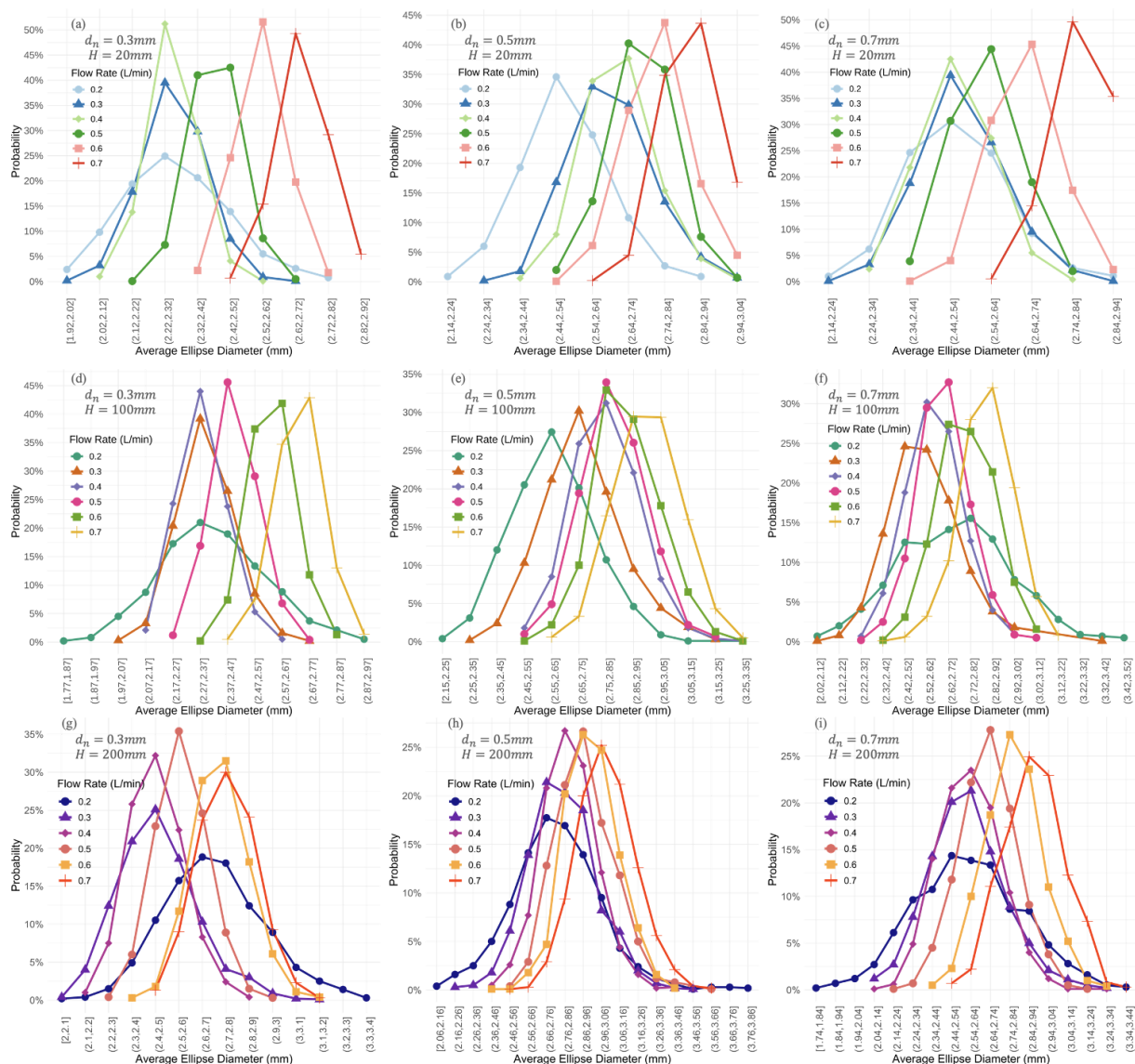


Fig. 11. Probability Density Distribution of Bubble Diameters.

2. Velocity and Trajectory

in Section IV B to accurately match and track them.

Fig. 12 shows the bubble velocities calculated using the bubble tracking method under different operating conditions. The results indicate that an increase in flow rate, bubble rise height, and nozzle diameter generally leads to an increase in the vertical velocity of the bubbles. However, the horizontal velocity remains relatively stable, showing minimal changes. This stability in horizontal velocity may be attributed to the geometric constraints of the experimental setup. In some cases (shown in Fig. 12(e, f, h, i)), no bubbles that met the criteria for tracking were identified following the method described in Section IV C 3. This occurred because the bubbles in these conditions lacked distinct characteristics and exhibited excessive overlap, which made it difficult for the model

Additionally, to investigate the effect of the constraints imposed by the rod bundle geometry on the bubble's horizontal and vertical motion, we conducted statistical calculations of bubble velocities in a free-rise environment (Table 5). The findings indicate that under the constraints of the rod bundle structure, the horizontal velocity of the bubbles significantly decreases, while the vertical velocity increases to some extent. This change may be attributed to the increased interaction between the bubbles and the surrounding water caused by the confined space within the rod bundle, which disrupts the bubbles' horizontal movement and enhances their vertical ascent. The increase in vertical velocity could be due to factors such as enhanced turbulence or flow acceleration within the confined channels of the rod bundle.

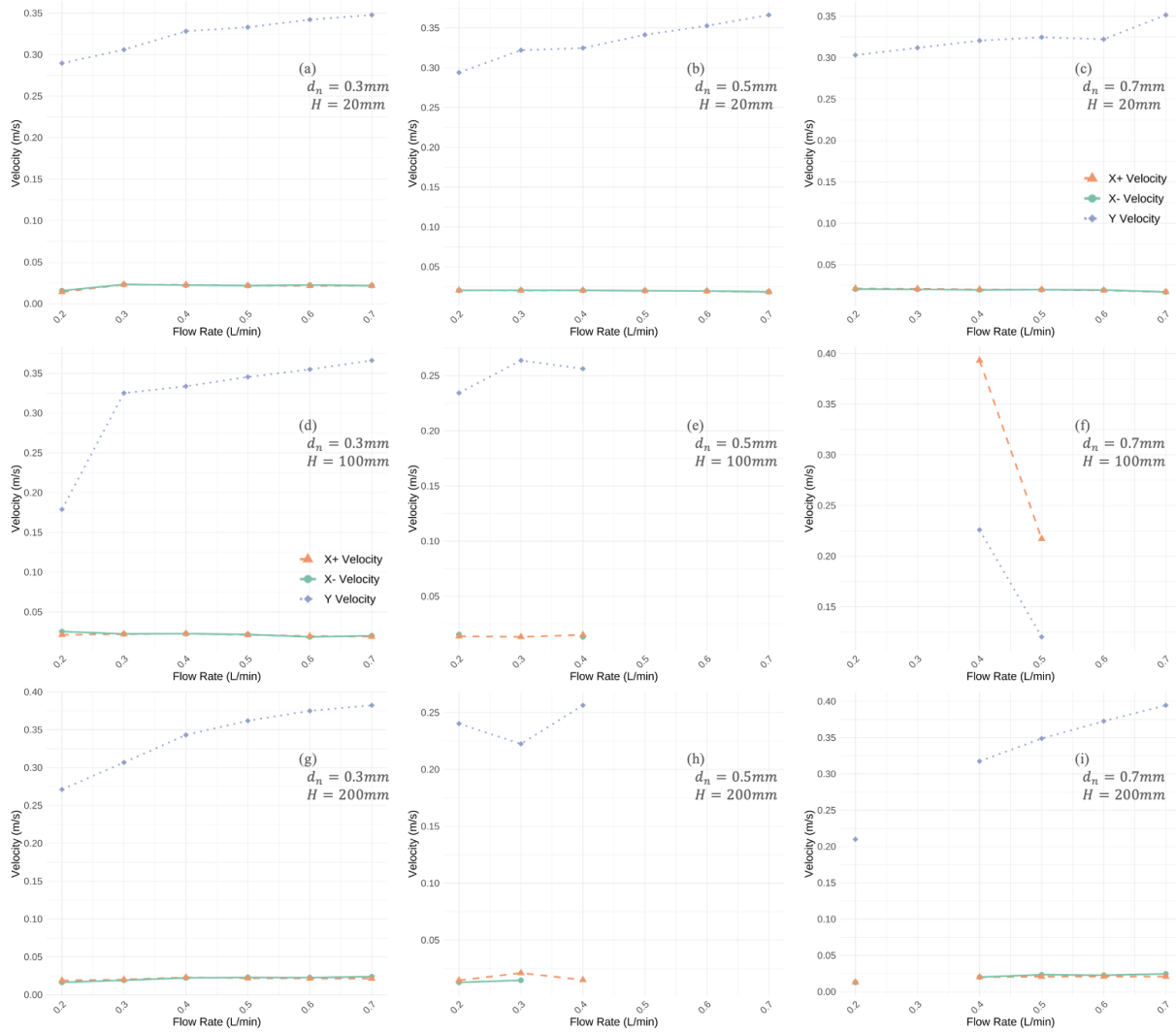


Fig. 12. Bubble Velocities under different operating conditions.

Table 5. Comparison of Bubble Velocities in Different Environments.

Type	velocityX+	velocityX-	velocityY
with rod bundles	0.0232	0.0226	0.342
without rod bundles	0.0477	0.0494	0.309

B. Void Fraction

Fig. 13 shows the void fraction calculated using three different methods under the specified operating conditions ($d_n=0.3\text{mm}$, $H=200\text{mm}$). As the air flow rate increases, the void fraction calculated using methods Fig. 13(a) and Fig. 13(b) exhibits an overall increasing trend. The slope initially increases and then decreases, meaning the change is rapid at first but becomes less pronounced later due to factors such as nozzle diameter limitation or other variables. Additionally, the void fraction calculated using the volume method shows a similar trend to that of the area method, but the values are consistently higher. This difference is likely due

to calculation errors arising from the assumption of bubbles as three-dimensional spheres or ellipsoids when using two-dimensional image data, as well as errors in calculating the cross-sectional area and volume of the target flow path. Since the volume is the target flow path for both methods in Fig. 13(b) and (c), a comparison shows that the trend based on air intake and bubble rise time is more stable and approaches a linear pattern. This may be due to using average bubble velocity to approximate overall air phase velocity, along with potential errors in flow meter accuracy.

Overall, the discrepancies between the three methods are relatively small, which further validates the feasibility of the proposed models and calculation methods.

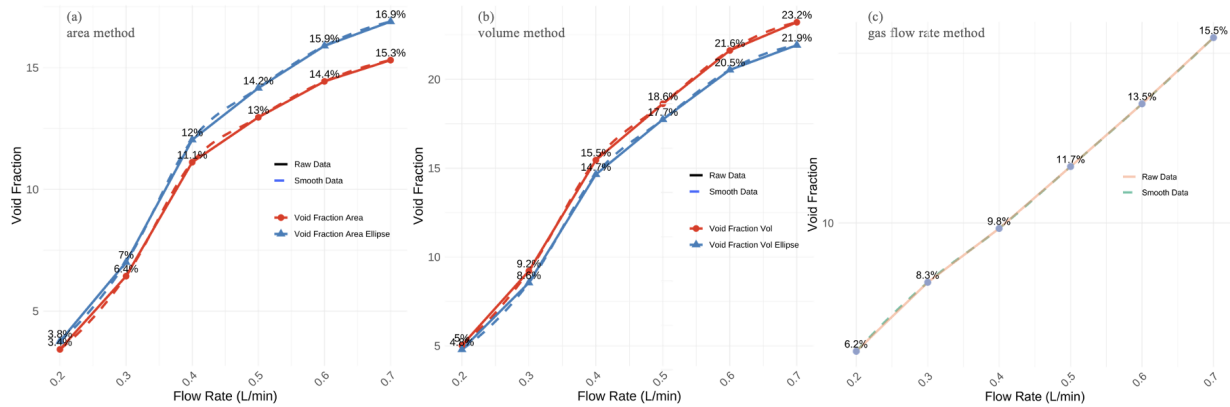


Fig. 13. Comparison of Void Fraction Calculated Using Three Different Methods.

Table 6. Comparison of Bubble Characteristic Parameters in Different Experimental Conditions

	Flow rate (L/min)						Nozzle diameter (mm)			Shooting height (mm)		
	0.2	0.3	0.4	0.5	0.6	0.7	0.3	0.5	0.7	20	100	200
avg_count	14.0030	25.4054	36.5780	42.5206	45.5033	46.8377	38.8357	33.3403	33.2480	44.0858	34.5245	26.8137
avg_diameter	2.5497	2.5376	2.5577	2.6409	2.7421	2.8392	2.4945	2.7871	2.6520	2.5745	2.6378	2.7213
avg_eccentricity	0.6523	0.6466	0.6416	0.6469	0.6549	0.6655	0.6385	0.6611	0.6543	0.6367	0.6418	0.6754
avg_velocity	0.2560	0.2966	0.3131	0.3020	0.3598	0.3711	0.3298	0.2900	0.3092	0.3341	0.2708	0.3147
min_velocity	0.0989	0.0591	0.0549	0.0140	0.0124	0.0124	0.0321	0.0834	0.0260	0.0240	0.0585	0.0624
max_velocity	1.4448	3.3491	3.6300	4.3609	4.3443	4.6136	3.8625	2.5702	3.9957	4.6600	2.1945	3.0350

C. Influence of Key Variables on Bubble Behavior

To more intuitively observe the impact of flow rate, nozzle diameter, and bubble rising height on the dynamic behavior of bubbles, we summarized the key bubble characteristic parameter values under different experimental conditions, as shown in Table 6.

With the increase in flow velocity, the number of bubbles significantly increases, with a faster initial growth rate that gradually stabilizes over time. This phenomenon is consistent with existing research, indicating that stronger shear forces and turbulence at higher flow velocities promote bubble generation and breakup. When the flow velocity reaches a certain threshold, the rates of bubble generation and breakup tend to balance, leading to a stabilization in bubble count. However, this study found that the bubble diameter generally exhibits an increasing trend, which differs from some studies that observed a decrease in bubble diameter with increasing flow velocity [24]. This discrepancy may be attributed to the dominant role of enhanced shear forces at high flow velocities, which promote bubble coalescence. Additionally, the irregularity of bubbles initially increases and then decreases at low flow velocities, but overall, it is less affected by flow velocity, likely due to the dynamic balance between surface tension and shear forces. The increase in bubble rise velocity at high flow velocities aligns with the energy transfer mechanism in fluid dynamics, suggesting that higher flow velocities provide more kinetic energy to the bubbles.

As the nozzle diameter increases, the number of bubbles decreases, with a faster initial reduction rate that gradually

stabilizes. This observation is consistent with existing research on the inhibitory effect of nozzle diameter on bubble generation. However, this study found that the bubble diameter peaks at a nozzle diameter of 0.5 mm and then decreases, which contrasts with some studies that reported a monotonic increase in bubble diameter with nozzle diameter. This nonlinear variation may be related to the interaction between shear forces and surface tension in fluid dynamics: smaller nozzle diameters result in higher fluid resistance, inhibiting bubble growth, while larger nozzle diameters may reduce shear forces due to expanded fluid channels, thereby affecting bubble stability. Furthermore, the irregularity and rise velocity of bubbles reach extreme values at a nozzle diameter of 0.5 mm, further highlighting the complex influence of nozzle diameter on bubble behavior.

As the bubble rise height increases, the number of bubbles gradually decreases, consistent with existing research on bubble reduction due to coalescence and breakup during ascent. However, this study found that the bubble diameter increases with rise height, which differs from some studies that observed a decreasing trend in the bubble diameter. This discrepancy may be related to experimental conditions, such as liquid viscosity and flow state. The irregularity of bubbles decreases with rise height, indicating that bubbles tend to stabilize during ascent, likely due to the dominant role of surface tension. Additionally, the bubble rise velocity initially decreases and then increases, possibly due to the dynamic balance between fluid resistance and changes in bubble shape.

Through the comprehensive and in-depth discussion of the experimental results, we have systematically grasped the per-

638 formance of bubble dynamics under different conditions and
639 the crucial roles played by various variables. On this basis,
640 it is necessary for us to summarize the entire research, ex-
641 tract conclusions with important theoretical and application
642 values.

643 VI. CONCLUSION

644 This study presents a comprehensive experimental investi-
645 gation into bubble dynamics within rod bundle sub-channels,
646 facilitated by the development of an integrated experimental
647 platform that combines both hardware and software systems.
648 The platform incorporates advanced deep learning-based im-
649 age processing methods, leveraging the improved Mask R-
650 CNN and DeepSORT algorithms for precise bubble detection,
651 segmentation, and tracking. This approach enables accurate
652 analysis of key dynamic parameters, such as bubble geome-
653 try, motion, and void fraction, in complex air-water two-phase
654 flow, providing valuable data for reactor system optimization.
655 The results reveal significant influences of key parameters
656 such as flow velocity, nozzle diameter, and bubble rise height
657 on bubble behavior, with bubble diameter and dynamics ex-
658 hibiting nonlinear variations. These variations are driven by
659 the interplay of shear forces, surface tension, and fluid re-
660 sistance. Additionally, the study effectively addresses the
661 complexities introduced by bubble clustering and rod interfe-
662 rence, overcoming challenges commonly encountered in tradi-
663 tional methods. The dynamic changes in bubble rise velocity,
664 including initial deceleration followed by acceleration, fur-
665 ther deepen our understanding of bubble behavior in rod bun-
666 dle sub-channels.
667 This study offers valuable theoretical insights for opti-
668 mizing heat and mass transfer efficiency in nuclear reactor
669 cooling systems but also offers valuable guidance for reac-
670 tor design, particularly for small modular reactors (SMRs).

671 The proposed method, combining advanced image process-
672 ing techniques, machine learning, and a robust hardware-
673 software platform, demonstrates substantial potential for fu-
674 ture research on multi-phase flow dynamics in complex sys-
675 tems. It holds promise for improving reactor safety, thermal-
676 hydraulic performance, and operational reliability.

677 VII. NOMENCLATURE

678	d_n	Nozzle diameter
679	H	Height difference from the bubble generator to the cam-
680		era
681	Q_g	Gas flow rate
682	E	Aspect ratio
683	w	Length of the major axes of the ellipse that has the same
684		normalized second central moments as the region
685	h	Length of the minor axes of the ellipse that has the same
686		normalized second central moments as the region
687	S	Number of pixels of the region
688	d	Spherical assumed bubble diameter
689	d_e	Ellipsoidal assumed bubble diameter
690	d_s	Sauter diameter
691	L_t	Height of the imaging segment measured using a scale
692	L_p	Camera's vertical resolution
693	w'	Length of the major axes of the ellipse from the contour-
694		point-based elliptical fitting
695	h'	Length of the minor axes of the ellipse from the contour-
696		point-based elliptical fitting
697	A	Total real cross-sectional area of the flow channel
698	V	Total real volume of the flow channel

699 VIII. BIBLIOGRAPHY

-
- 700 [1] Han X, Duan G, Wang J. Two-group bubble interfacial
701 area concentration correlation for upward bubbly to churn
702 flows in vertical rod bundle flow channels. *International*
703 *Journal of Heat and Mass Transfer* **202**, 123742 (2022).
704 [doi:10.1016/j.ijheatmasstransfer.2022.123742](https://doi.org/10.1016/j.ijheatmasstransfer.2022.123742)
- 705 [2] Katono K, Fujimoto K, Arai T, et al. Experimental Inves-
706 tigation of Rod Pitch Effect on Void Fraction in 5×5
707 Rod-bundle under Elevated Pressure Conditions. *International*
708 *Journal of Heat and Mass Transfer* **195**, 123035 (2022).
709 [doi:10.1016/j.ijheatmasstransfer.2022.123035](https://doi.org/10.1016/j.ijheatmasstransfer.2022.123035)
- 710 [3] Li B. Preliminary Analysis of the Impact of Cavitation
711 on Nuclear Reactor Safety. *Science and Technology Inno-*
712 *vation Herald* **13**, 63+65 (2016). [doi:10.16660/j.cnki.1674-](https://doi.org/10.16660/j.cnki.1674-098X.2016.07.063)
713 [098X.2016.07.063](https://doi.org/10.16660/j.cnki.1674-098X.2016.07.063)
- 714 [4] Yan H, Zhang H, Liu L, et al. Effect of gas flow rate and nozzle
715 diameter on bubble size and shape distributions in bubble col-
716 umn. *Transactions of Nonferrous Metals Society of China* **34**,
717 1710–1720 (2024). [doi:10.1016/S1003-6326\(24\)66501-5](https://doi.org/10.1016/S1003-6326(24)66501-5)
- 718 [5] Taş S. A comprehensive review of numerical and ex-
719 perimental research on the thermal-hydraulics of two-
720 phase flows in vertical rod bundles. *International Jour-*
721 *nal of Heat and Mass Transfer* **221**, 125053 (2023).
722 [doi:10.1016/j.ijheatmasstransfer.2023.125053](https://doi.org/10.1016/j.ijheatmasstransfer.2023.125053)
- 723 [6] WEN D, CHEN W, YIN J, et al. Overlapping bubble detection
724 and tracking method based on convolutional Neural network
725 and Kalman Filter. *Chemical Engineering Science* **263**, 118059
726 (2022). [doi:10.1016/j.ces.2022.118059](https://doi.org/10.1016/j.ces.2022.118059)
- 727 [7] Liu S, Liu L, Gu H, et al. Experimental study of gas-liquid
728 flow patterns and void fraction in prototype 5×5 rod bun-
729 dle channel using wire-mesh sensor. *Annals of Nuclear Energy*
730 **171**, 109022 (2022). [doi:10.1016/j.anucene.2022.109022](https://doi.org/10.1016/j.anucene.2022.109022)
- 731 [8] Zafari S, Eerola T, Sampo J, et al. Segmentation of Overlap-
732 ping Elliptical Objects in Silhouette Images, in *IEEE Trans-*
733 *actions on Image Processing*, vol. 24, no. 12, pp. 5942–5952, Dec.
734 2015, [doi:10.1109/TIP.2015.2492828](https://doi.org/10.1109/TIP.2015.2492828).
- 735 [9] Chen W, Huang G, Hu Y, et al. Experimental study on contin-
736 uous spectrum bubble generator with a new overlapping bub-
737 bles image processing technique. *Chemical Engineering Sci-*
738 *ence* **254**, 117613 (2022). [doi:10.1016/j.ces.2022.117613](https://doi.org/10.1016/j.ces.2022.117613)
- 739 [10] Zhang H, Lü X, Li H, et al. Light Field Deconvolution Algo-

- rithm for Three-Dimensional Plasma Reconstruction. *Acta Optica Sinica* **43**, 0715001 (2022). doi:10.3788/AOS221789
- [11] SOIBAM J, SCHEIFF V, ASLANIDOU I, et al. Application of deep learning for segmentation of bubble dynamics in subcooled boiling. *International Journal of Multiphase Flow* **169**, 104589 (2023). doi:10.1016/j.ijmultiphaseflow.2023.104589
- [12] ZHOU W, MIWA S, TSUJIMURA R, et al. Bubble feature extraction in subcooled flow boiling using AI-based object detection and tracking techniques. *International Journal of Heat and Mass Transfer* **222**, 125188 (2024). doi:10.1016/j.ijheatmasstransfer.2024.125188
- [13] CUI Y, LI C, ZHANG W, et al. A deep learning-based image processing method for bubble detection, segmentation, and shape reconstruction in high gas holdup sub-millimeter bubbly flows. *Chemical Engineering Journal* **449**, 137859 (2022). doi:10.1016/j.cej.2022.137859
- [14] Shi J, You L, Wang Y, et al. Deep learning based method for dynamic tracking of bubbles in microfluidic gas-driven water experiments. *Geoenery Science and Engineering* **243**, 21339 (2024). doi:10.1016/j.geoen.2024.213391
- [15] KURIMOTO R, NEUMEISTER R F, KOMINE R, et al. Shapes and terminal velocities of single bubbles rising through fiber bundle in stagnant water. *Chemical Engineering Science* **299**, 120557 (2024). doi:10.1016/j.ces.2024.120557
- [16] WANG K, JUNYA I, LI C, et al. Invariant aluminum CHF under electron beam irradiation conditions for downward-facing flow boiling. *Applied Thermal Engineering* **220**, 119810 (2022). doi:10.1016/j.applthermaleng.2022.119810
- [17] HE K, GKIOXARI G, DOLLAR P, et al. Mask R-CNN, 2017 IEEE International Conference on Computer Vision (ICCV). Venice: IEEE, 2017: 2980-2988[2024-08-24], doi:/10.1109/ICCV.2017.322.
- [18] Chen J, Kao S, He H, et al. Run, Don't walk: chasing higher FLOPS for faster neural networks. In: *Conference on Computer Vision and Pattern Recognition*, pp. 12021–12031. doi:10.1109/CVPR52729.2023.01157
- [19] Kim Y, Park H. Deep learning-based automated and universal bubble detection and mask extraction in complex two-phase flows. *Sci Rep* **11**, 8940 (2021). doi:10.1038/s41598-021-88334-0
- [20] Wojke N, Bewley A, Paulus D. Simple online and realtime tracking with a deep association metric, 2017 IEEE International Conference on Image Processing (ICIP), Beijing, China, 2017, pp. 3645-3649, doi:10.1109/ICIP.2017.8296962.
- [21] Tan W, Liu X, Wu D, et al. Measurement of Bubble Group Characteristics of Gas-Liquid Two-Phase Flow by Laser Cross Section Imaging. *Acta Optica Sinica* **42**, 1510001 (2022). doi:10.3788/AOS202242.1510001
- [22] YAN C, YAN C, SUN L, et al. Characteristics of void fraction distribution of bubbly flow in inclined channels. *CIESC Journal* **65**, 855-861 (2014). doi:10.3969/j.issn.0438-1157.2014.03.013
- [23] Xue T, Li S, Li Z. Characteristics Measurement of Dense Bubbly Flow based on Laser Scanning, 2022 IEEE International Instrumentation and Measurement Technology Conference (I2MTC), Ottawa, ON, Canada, 2022, pp. 1-5, doi:10.1109/I2MTC48687.2022.9806520.
- [24] Qian K, Wang Z. Simulation of Bubble Growth in Transverse Flow in Horizontal Pipe. *Modeling and Simulation* **10**, 424-434 (2022). doi:10.12677/MOS.2021.102043.